

Active boundary layers

Jérôme Hardoüin,^{1,2} Justine Laurent,³ Teresa Lopez-Leon,⁴ Jordi Ignés-Mullol,^{1,2} and Francesc Sagués^{1,2}

¹*Departament de Química Física, Universitat de Barcelona, 08028 Barcelona, Spain*

²*Institute of Nanoscience and Nanotechnology, Universitat de Barcelona, 08028 Barcelona, Spain*

³*Laboratoire PMMH, UMR CNRS 7083, ESPCI Paris, PSL Research University, 75005 Paris, France*

⁴*Laboratoire Gulliver, UMR CNRS 7636, ESPCI Paris, PSL Research University, 75005 Paris, France*

(Dated: December 22, 2024)

The role of boundary layers in conventional liquid crystals is commonly subsumed in their anchoring on confining walls. In the classical view, anchoring enslaves the orientational field of the passive material under equilibrium conditions. In this work, we experimentally explore the role of confining walls in the behavior of an active nematic. We find that, under slip boundary conditions, the wall induces the accumulation of negatively charged topological defects in its vicinity, resulting in the formation of a topological boundary layer that polarizes the wall. While the dynamics of wall and bulk defects are decoupled, we find that the active boundary layer influences the overall dynamics of the system, to the point of fully controlling the behavior of the active nematic in situations of strong confinement. Finally, we show that wall defects exhibit behaviors that are essentially different from those of their bulk counterparts, such as high motility or the ability to recombine with another defect of like-sign topological charge. These exotic behaviors result from a change of symmetry induced by the wall in the director field around the defect. Finally, we show that the collective dynamics of wall defects can be described in terms of a one-dimensional Kuramoto-Sivashinsky-like description of spatio-temporal chaos.

I. INTRODUCTION

The concept of boundary layer is fundamental in Physics, from fluid dynamics [1] to soft matter [2]. It refers to the part of the flow that is close to a boundary, featuring built up slip velocities associated to localized profiles of scalar fields, like pressure, temperature, solute concentration or ionic charge density. Although the length scale spanned by such boundary layers is much smaller than any macroscopic length, the details of the interfacial transport processes entirely control the distant fluid dynamics. Here, we reveal the existence of a new type of boundary layer in a confined Active Nematic (AN) [3], which we call *active boundary layer* (ABL).

In this work, ANs are experimentally realized by the self-assembly of filamentous bundles of microtubules and molecular motors at the water/oil interface [4–7], which form an active ordered layer populated by motile topological defects. These defects are singularities in the orientational field endowed with topological indices bearing characteristics similar to those of electric charges. Stressing this resemblance, and expanding the conventional notion of charged interfaces, we demonstrate that ANs [3, 8, 9] engender ABLs that become topologically polarized by accumulating equal-sign orientational defects.

Experiments [4, 6, 10–13] and theoretical models [14–20] show that ANs feature a balanced population of positive, self-propelling, and negative, passively-entrained, semi-integer defects that continuously unbind and recombine, resulting in a turbulent mixing regime [12, 21–24]. Different from this traditional view, we show here that ABLs are exclusively populated by negative defects. When analyzed individually, these boundary defects display differences with respect to their bulk counterparts, both in terms of their motility, symmetries, and

built-up stresses. Remarkably, we identify recombination events between equal-sign defects residing at the boundary. While the AN in the boundary layer appears largely protected from the rest of the active preparation, the reverse is not true. For instance, by pinning defects at specific wall locations, we demonstrate that the boundary layer enslaves the rest of the material by ejecting streaming jets that determine the system-wide flows. Finally, by going from the individual to the collective dynamics of boundary defects, we show that their concerted effect echoes a purely one-dimensional Kuramoto-Sivashinsky (KS)-like description of spatio-temporal chaos [25].

II. MATERIALS AND METHODS

A. Active gel preparation

Microtubules (MTs) were polymerized from heterodimeric (ζ, β)-tubulin from bovine brain (Biomaterials Facility, Brandeis University MRSEC, Waltham, MA) as described previously [7] in order to obtain MTs with an average length $1 - 2 \mu\text{m}$. The MTs were mixed with a suspension of kinesin motor clusters (an average of two motors per cluster) in order to act as motile cross-linkers, and Adenosine Triphosphate (ATP) to drive the activity. The non-adsorbing polymer Poly-ethylene glycol (PEG, 20 kDa) promoted the formation of filament bundles through depletion. An enzymatic ATP regenerator system ensured the duration of activity for several hours. A summary of all relevant components of the active gel is summarized in Table I.

B. Grid Manufacturing

High resolution polymeric grids of thickness $100\mu\text{m}$ were printed using a Nanoscribe GT Photonic Professional two-photon polymerization printer (Nanoscribe GmbH, Germany) and a $25\times$ objective. The grids were directly printed on silicon substrates without any preparation to avoid adhesion of the resist to the substrate. After printing, the grids are bound to a vertical glass capillary, carefully detached, and washed. Each grid contains different channel geometries so that simultaneous experiments can be performed with the same active nematic preparation, thus ensuring reproducibility.

C. Active nematic preparation

A PDMS block with a cylindrical well 5 mm in diameter and in depth is glued on a bioinert glass substrated coated with a Poly-acrylamide brush. $2\mu\text{L}$ of the active gel is deposited on the substrate and immediately covered with $100\mu\text{L}$ of 100 cS silicone oil. A few minutes after this preparation, a AN layer forms at the aqueous/oil interface. The required polymeric grid is subsequently submerged in the well using a micromanipulator until it contacts the interface and placed until capillary distortions are minimized.

D. Imaging and image processing

Images were acquired using a laser scanning confocal microscope Leica TCS SP2 AOBS with a $10\times$ objective at typical frame rate of 1 image per second. Background correction and kymograph computation were performed with the software ImageJ [26]. The local nematic director, \mathbf{n} , and nematic tensor, \mathbf{Q} , where computed using custom Matlab scripts as detailed by Ellis *et al.* [27]. In brief, the local alignment of the microtubules is inferred using coherence-enhanced diffusion filtering. Noise is first removed from the raw images by means of a Gaussian blur filter with standard deviation σ . The local "molecular director", \mathbf{u} , is obtained, at the pixel level, by finding the direction along which the fluorescence intensity is most homogeneous. The resulting field $u(x, y)$ is subsequently smoothed by means of a Gaussian blur with standard deviation ρ , and used to obtain the local matrices $\mathbf{M} = \langle \mathbf{u} \otimes \mathbf{u} - \frac{1}{2}\mathbb{1} \rangle_\beta$ using an ensemble average within a disk of radius β pixels. These matrices are finally diagonalized choosing, at each pixel, the eigenvector \mathbf{n} , with the largest eigenvalue, S , which will be the nematic director field and order parameter, respectively, and from which the tensor order parameter is computed as $\mathbf{Q} = S \langle \mathbf{n} \otimes \mathbf{n} - \frac{1}{2}\mathbb{1} \rangle$. The three filtering parameters are manually adjusted by visual inspection of the resulting director field. For the current experiments, we find that typical optimal values are $\sigma = 0.5\text{px}$, $\rho = 15\text{px}$, and

$\beta = 5.5\text{px}$. Finally, the local active stress is computed as $\mathbf{f} \sim \nabla \cdot \mathbf{Q}$.

Compound	Stock solution	v/V_{total}
PEG	12 % <i>w.vol</i> ⁻¹	0.139
PEP	200 mM	0.139
High-salt M2B	69 mM MgCl ₂	0.05
Trolox	20 mM	0.104
ATP	50 mM	0.03
Catalase	3.5 mg.ml ⁻¹	0.012
Glucose	300 mg.ml ⁻¹	0.012
Glucose Oxydase	20 mg.ml ⁻¹	0.012
PK/LDH	600 – 1000 units.ml ⁻¹	0.03
DTT	0.5 M	0.012
Streptavidin	0.352 mg.ml ⁻¹	0.023
Kinesin	0.07 mg.ml ⁻¹	0.234
Microtubules	6 mg.ml ⁻¹	0.167
Pluronic	17 %	0.027

TABLE I. Composition of all stock solutions, and their volume fraction in the final mixture.

E. KSE simulations

The simulation presented in Fig. 5 (a) was performed using an open source simulation code[28] solving the following equation:

$$\psi_t = -\psi\psi_x - \psi_{xx} - \psi_{xxx}, \quad (1)$$

using periodic boundary conditions on $[0, 32\pi]$ and $\psi(x, 0) = \cos(x/16)$ as an initial condition. The computation is based on the Fourier Transform of ψ , $v = \text{fft}(\psi)$. The final plot shown in Fig. 5 (a) corresponds to $\psi(x, t) = \text{Re}(\text{ifft}(v))$ where *ifft* is the inverse Fourier Transform operator. It was computed on a discrete domain of $N = 1024$ points and 6000 time steps. For representation in Fig. 5, only one in six time steps are plotted.

III. RESULTS

A. Self-assembly of active boundary layers

We begin by describing the structure of the steady-state ABLs that form at the inner and outer walls of annular-shaped channels. This geometry is chosen to avoid end-effects, while channels are wide enough to ensure that the dynamics of the boundary layers at either wall are effectively decoupled. In our system, a few microliters of the kinesin/tubulin active mixture is placed in a custom-made open pool 5 mm in diameter, and subsequently covered with 100 cSt silicon oil (see. Methods) [6, 7]. Confining micro-platforms are set in contact with the oil/water interface once the AN is formed. They are flat, rigid polymeric slabs with embodied micro-channels manufactured with three-dimensional micro-printing techniques (see S.I.).

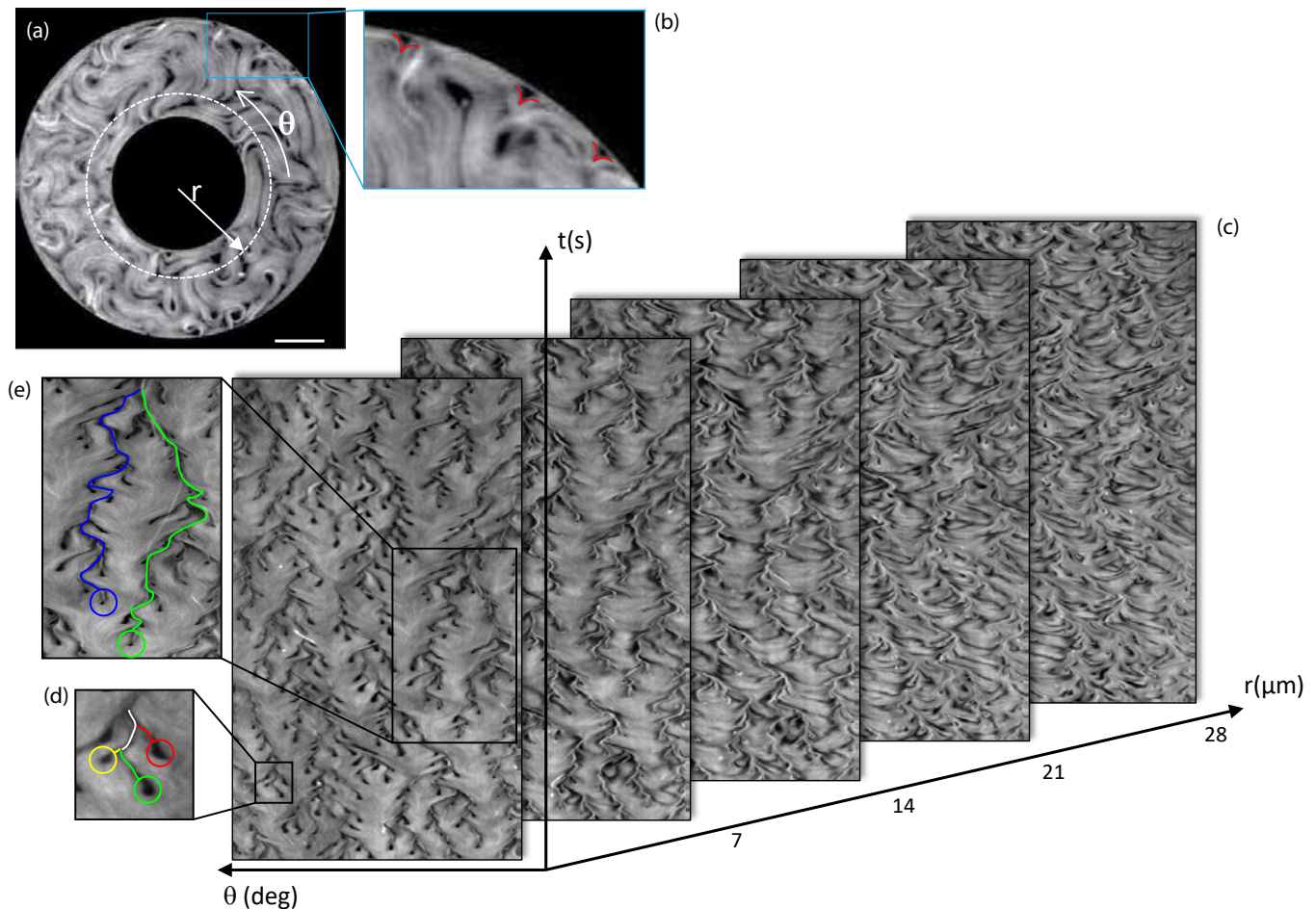


FIG. 1. Active nematic dynamics close to a wall. (a) Fluorescence micrograph of the active nematic flowing inside an annular channel (see Movie S1). Scale bar: $100 \mu\text{m}$. (b) Magnified image showing three of the $-1/2$ defects that form the outer ABL. (c) Kymographs corresponding to the fluorescence intensity profile along circumferences (θ spanning from 0 to 360 degrees) at increasing distances from the inner channel wall, as indicated in (a). We consider the inner wall to be at $r = 0$. For each plot, circular profiles at different times are stacked vertically, for a total duration of 300 s. (d) Region of the inner-most kymograph showing three "blossoms" that merge into a single "branch". (e) Region of the inner-most kymograph showing the long-range attraction between branches.

Micro-channels induce lateral confinement of the quasi-two-dimensional AN, and impose planar anchoring conditions on the active filaments and favorable slip velocity conditions along the channel walls [7]. Since aligned extensile ANs are prone to bend-like instabilities [24, 29, 30] that terminate with the unbinding of defect pairs [4, 17], walls become preferential sites for defect nucleation [7, 31, 32].

In Fig. 1, we show data for an annulus of $200 \mu\text{m}$ width. Fluorescence micrographs display the typical active turbulence regime away from the walls (Fig. 1a). Close to the inner and outer walls, a new structure and behavior emerges in the form of boundary defects, whose number and position change with time but never leave the boundary region. They are reminiscent of the $-1/2$ defects normally found in AN, with a hyperbolic-shaped core region devoid of fluorescent filaments (Fig. 1b). In

order to visualize the dynamics of these boundary defects, we have built kymographs by measuring the fluorescence intensity along a circumference divided in 360 equal bins, and we have stacked vertically the resulting pixel lines obtained at increasing times. We have performed this measurement at different distances from the inner channel wall, illustrating this way the penetration depth of the ABL (Fig. 1c).

Close to the wall ($r \simeq 0$), kymographs appear anisotropically patterned, with tree-like lines, separated by smoother regions of relatively uniform intensity. Branches originate from dark "blossoms" that pop up from uniform regions, and correspond to spontaneous events of boundary defect nucleation, while branching points correspond to defect merging events (Fig. 1d). Branches are often short, corresponding to ephemeral defects, although the existence of long-lived branches

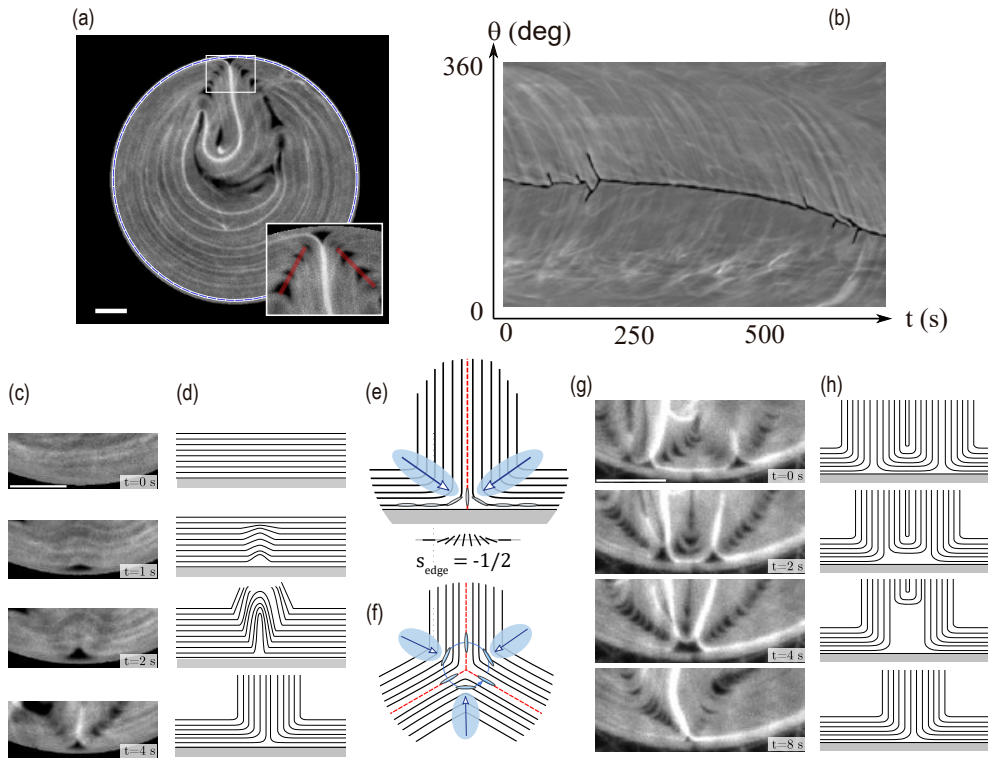


FIG. 2. Birth and death of wall defects. (a) Fluorescence micrograph of the active nematic evolving inside a circular pool (see Movie S2). In the inset, a magnified view of the region around the single wall defect showing the bright plume and highlighting in red the lateral "cracks" (see text). (b) Kymograph built with the grayscale intensity along the blue dashed circumference in (a). (c) Experimental time-lapse of a wall-defect nucleation in the disk. (d) Corresponding sketch of the dynamics. Structure and active forces of a wall (e) and a bulk (f) negative defect. The determination of the topological charge is shown for the surface defect. Red dotted lines indicate the symmetry axes and blue areas are the regions with higher active stress. Blue arrows mark the direction of the resulting active force. (g) Experimental time-lapse of the merging between two wall-defects in the same system. (h) Corresponding sketch of the dynamics. In (c-h), the confining wall is located at the bottom. Scale bars, $100 \mu\text{m}$.

are the signature of resident wall defects that experience long-distance attraction (Fig. 1e). This hierarchical dynamics gradually vanishes away from the wall, and around $25 \mu\text{m}$ away from it kymographs become as structureless as at the center of the channel, corresponding to the typical structure of AN in unconfined systems. The situation is similar at the inner and at the outer annulus walls, and also near flat walls in rectangular channels (Fig. S1), indicating that the ABLs form regardless of the channel geometry.

B. Emergence and interaction between wall defects

1. Structure and dynamics of wall defects

Isolated wall-defects are best tracked in disk-shaped pools, where we the AN displays rather uniform textures and system-wide quasi-laminar flows (Fig. 2a). This is an indication of the presence of very few wall defects, often a

single one for most of the observation time, with the occasional emergence and quick annihilation of additional wall defects. Corresponding kymograph of the boundary texture display scarce blooms and branches (Fig. 2b). As observed in the kymograph, the single wall defect can either fluctuate around a random fixed position for an undetermined period of time (first 250s in Fig. 2b and S2a) or drift autonomously along the circular boundary, clockwise or counter-clockwise handedness having similar likelihood (from 250s onwards in Fig. 2b and S2b). Occasionally, this dynamics is interrupted by brief episodes of defect nucleation, followed by injection of a positive defect into the bulk and merging of the newborn negative defect with the preexisting one (Fig. S2c).

The birth of a wall defect is observed as a time lapse in Fig. 2c and schematically depicted in Fig. 2d. After nucleation and unbinding, the core of the defect that remains at the wall accumulates an edge charge $-1/2$ (Fig. 2c,d) and the conventional three-fold is transformed into a bilateral symmetry about a plane perpendicular to the

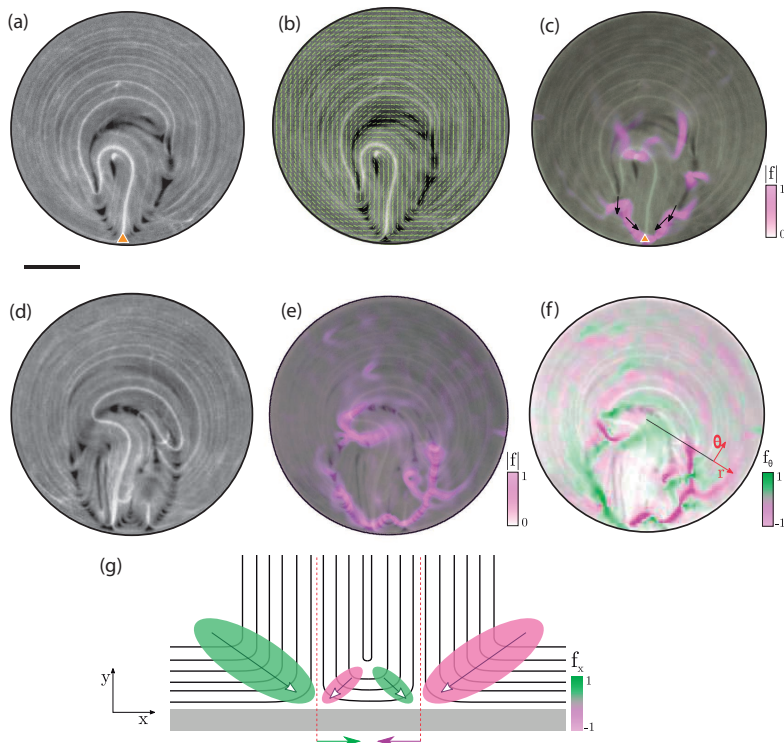


FIG. 3. Active forces organized by boundary layer defects. (a) Fluorescence micrograph of an active nematic confined in a disk. The orange triangle indicates the location of a wall defect. (b) Corresponding director field overlaid on top of the fluorescence image. (c) Active force map overlaid (in pink) on top of the fluorescence image. Arrows indicate the direction of the force, while the color intensity maps the magnitude of the force. (d) Fluorescence micrograph of the system with two neighboring wall defects. (e) Magnitude of the active force f overlaid (in pink) on top of the fluorescence micrograph. (f) Projection of f in the azimuthal (θ) direction. The color code is green for counter-clockwise (CW) and pink for clockwise (CCW) force. (g) Sketch of the orientational field and the force map in the vicinity of the two neighboring wall defects prior to annihilation. Scale bar $100 \mu\text{m}$.

wall (Fig. 2e). Because of this symmetry, stress accumulates along the symmetry axis of wall defects, hindering their escape from the ABL. The defect core is prolonged by a plume of high-density fluorescent filaments (Fig. 2a), and flanked by bent filaments where the orientational field turns by $\pi/2$ (Fig. 2e). This amount is larger than the standard $\pi/3$ bending of filaments in bulk $-1/2$ defects (Fig. 2f), resulting in higher elastic stresses. Because of their rigidity, filaments cannot accommodate the higher curvature, and additional void regions form. We call these flanking structures *cracks* (Fig. 2a), which are prevented from fading away by periodically unbinding additional $+1/2$ and $-1/2$ bulk defect pairs to release the accumulated elastic energy. Annihilation of equal sign wall defects is facilitated by the intercalation of a $+1/2$ defect that is progressively extruded into the bulk AN, as negative wall defects overlap and finally reconstitute a single boundary defect (Fig. 2g,h).

2. Force balance within the active boundary layer

We pursue this description in a more quantitative basis by assessing the active forces acting on single and neighboring pairs of wall defects. We first evaluate the tensor order parameter from the nematic director field extracted from fluorescence micrographs, and we further compute its local gradients to map the local active forces [27]. In S. I. we give details on how this method is implemented. Figure 3 illustrates the situation for a single defect (Fig. 3a-c) and for a pair of defects prior to recombination (Fig. 3d-g). In the first scenario, a nearly symmetric force distribution self-organizes along the cracks that emanate from isolated wall defects, protecting them and keeping them confined within the boundary layer (see Fig. 3c). On the other hand, when two wall defects approach (Fig. 3d), the force distribution is no longer symmetric around each defect, and a net attractive force between the defects builds up, as observed in the map of the active force component along the boundary (Fig. 3e,f). A sketch illustrating this force imbalance is presented in Fig. 3g.

We have also looked for signatures of a coupling be-

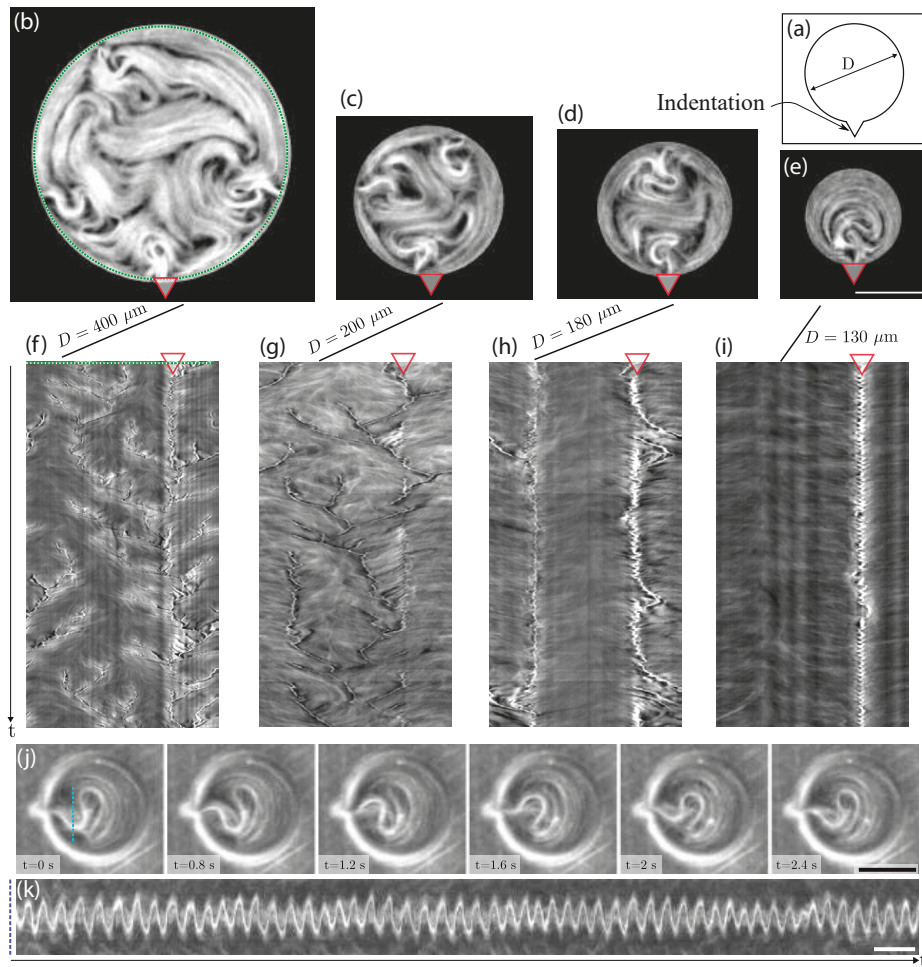


FIG. 4. Wall-pinning determines defect dynamics. (a) Sketch of the corrugated disk geometry. The indentation is a triangle with a fixed width and height of $10 \mu\text{m}$. (b-e) Fluorescence micrographs of active nematics confined in corrugated disks with $D = 400, 200, 180, 130 \mu\text{m}$, respectively (see Movie S3). The red triangle locates the indentation. Scale bar: $100 \mu\text{m}$. (f-i) Space-time plots along the perimeter of each disk. Total elapsed time is 300 s. The red triangles locate the position of the indentation. (j) Time-lapse of the periodic oscillation of active nematics confined in a $130 \mu\text{m}$ corrugated disk. The indentation is located to the left side of the disk. Scale bar: $100 \mu\text{m}$. (k) Space-time plot along the blue dotted line in (j). Scale bar: 10 s.

tween wall defect nucleation events and the evolution of the stress in the whole system. We have found that, although nucleation events only occur when the average tangential stress in the system is either a maximum or a minimum in the course of time, wall defects nucleate randomly (Fig. S3a,b). This is a remarkable difference with earlier work by Opathalage et al. [32] on an AN inside circular cavities where ephemeral boundary defects nucleated periodically, strongly correlated with the oscillations of the stress in the whole system (Fig. S3a,b). The difference in boundary conditions for the active flow in the two systems, no-slip in the earlier work [32] and slip, or partial slip, in the present case, effectively allows wall defects in our system to form an ABL that evolves mostly decoupled from the bulk active material.

3. Pinning of wall defects and entrainment of bulk active flows

Before considering collective effects, we will demonstrate how the bulk active flows can be controlled by direct intervention in the structure of the ABL. This is achieved after modifying the normally smooth disk boundary to introduce an indentation much smaller than the typical coherence length of the AN, in order to anchor wall defects at predefined locations. Here, we use indentations that are ten times smaller than such typical length scales (around $100 \mu\text{m}$ [24]). This minimal intervention offers remarkable perspectives towards the large scale control of the AN, as illustrated in Fig. 4 for different disk sizes.

Under the experimental conditions in that experiment,

the bulk dynamics is rather chaotic for the largest disk size of $400\ \mu\text{m}$ diameter (Fig. 4b). A considerable number of wall defects nucleate randomly, besides the one emerging from the corrugation, as can be seen in the corresponding kymograph of the fluorescence intensity along the boundary perimeter. The average number of wall defects decreases with the disk size, while the indentation acts a defect attractor where many dynamic branches collapse (Fig. 4c,g). As the disk diameter reaches $180\ \mu\text{m}$, the ABL starts to determine the overall flow. In this case, nucleation of additional wall defects is mostly limited to a single defect across the diameter from the corrugation (Fig. 4d), as can be observed in the corresponding kymograph, where only a few additional, short-lived branches are observed (Fig. 4h). Finally, when the diameter is decreased below $130\ \mu\text{m}$ (Fig. 4e,i) a single pinned wall defect is observed. A fluorescent plume, with high concentration of active filaments, constantly emanates from the corrugation, without additional disturbances in the ABL. This leads to periodic oscillations (Fig. 4j,k) of this plume, which is reminiscent of the cilia-like beating identified for bundled microtubules by Sanchez et al. [33].

C. Wall defects: Collective behavior

Finally, we will analyze the collective dynamics of wall defects, characterized by the merging tree-shaped spatio-temporal patterns presented in Fig. 1. We will show that these spatio-temporal patterns are reminiscent of those predicted by the Kuramoto Sivashinski equation (KSE). The latter is the simplest envelope equation that yields spatio-temporal chaos [25], and has been applied in the study of pattern formation in a wide variety of condensed matter systems [25, 34–40].

The one-dimensional nature of the KSE suggests a direct mapping with the defects in the ABL of confined ANs. In fact, the spatiotemporal patterns emerging in KSE simulations bear a striking resemblance with the kymographs from the ABL (Fig. 5). The most distinctive feature of KSE chaos is its spectrum of spatial fluctuations, considered as a proxy of the energy spectrum. It is mainly characterized by a well-defined peak at short wavelengths followed by a short-range scaling at intermediate wave-numbers, k , of the form k^{-4} . Previous publications successfully recovered the shape of KSE spectra from the collective interactions of long-lived fluctuations [41], thereby evidencing the predominant role of these objects in the energy mitigation process [42]. In unconfined ANs, substantial work has recently aimed at elucidating the kinetic energy regulation, so far mostly in simulations [21, 23]. In the vicinity of a boundary, the existence of wall defects and their special collective dynamics will *a priori* result in a different spectrum that should resemble the KSE provided our analogy remains valid for this observable.

As a first approach, we directly compute the spectrum

of spatial fluctuations from the fluorescence intensity profile along a wall in an annular channel. We begin by computing the two-point correlation function of the fluorescence intensity at each time, $C(x;t)$, and average it over the duration of the experiment to obtain $C(x)$. Finally, we perform a spectral analysis by computing the Fourier transform of $C(x)$, which is assimilated to the energy spectrum in simulations of the KSE [41]. In Fig. 5, we compare this analysis performed on simulations of the KSE (see S.I. and Fig. 5(a-d)) and on experimental fluorescence profiles from the inner wall of an annular channel (Fig. 5(e-h)).

Qualitatively, KSE and experimental AN spectra do show similarities (Fig. 5 (d) and (h)), with the existence of a peak followed by a power-law decay. Generic patterns of localized structures, shown in Fig. 5 (a) and (e), are indeed similar in both cases, albeit detailed textures look somewhat different. Defect-based patterns in the AN seem to contain many more short-lived branches than in the KS-based plots. An excess of such short traces may overshadow the regularity of the tree arrangement, and degrade the spatial correlation, as seen in Fig. 5 (c and g). Overall, although the detailed collective dynamics of wall defects are strikingly similar to that of localized structures in KSE chaos, a more refined experimental study remains to be done to faithfully compare the consequences in terms of energy distribution.

On the other hand, the framework of the KSE has also been successfully employed to study spatio-temporal chaos using simple statistical interactions between short-lived and long-lived structures, which we will relate here to the structures emerging in kymographs of the ABL. In this alternative analysis of kymographs, we begin by discriminating defect trajectories in terms of their persistence, measured by the time between nucleation and merging (Fig. S4). By performing a statistical analysis of these lifetimes, we observe a peak at short times (many ephemeral trajectories) and a long-tailed distribution, since trajectories of all durations are possible (Fig. S5). Even durations longer than our observation time are observed, as evidenced by the peak at 300 s (the duration of this experiment). We next defined a threshold time t_{th} to classify this broad dispersion in trail lengths according to whether their duration from nucleation until merging is shorter or longer than t_{th} , calling the short and long-lived trails *branches* and *trees*, respectively. For the analysis shown in Fig. 6, corresponding to the kymograph for the inner wall of an annular ring, we have set $t_{th} = 50\text{s}$.

Once the populations are classified, we proceed to analyze the geometry of the spatio-temporal patterns by measuring the equal-time separation of neighboring trails (Fig. 6(c)). When all trails are included, the distribution features two partially-overlapped peaks. The first one at $\delta = 42 \pm 10\ \mu\text{m}$ is indicative of the most likely trail-trail generic distance, while the second maximum at $\delta_{bt} = 115 \pm 10\ \mu\text{m}$ identifies a characteristic branch-tree separation. By analyzing the distribution

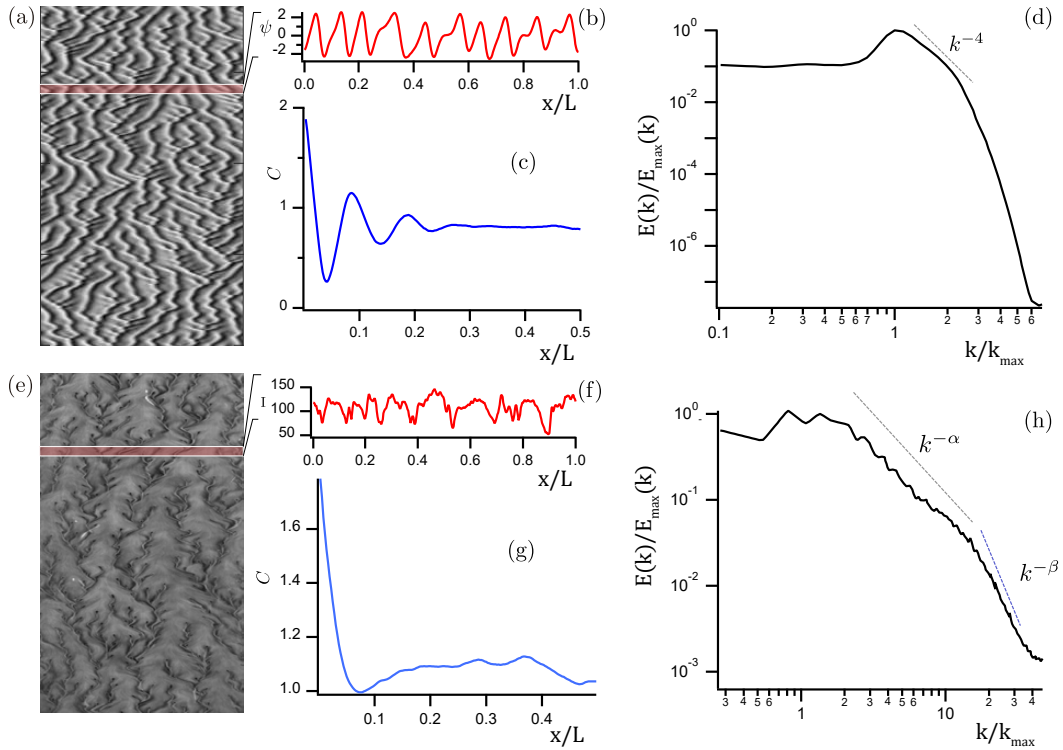


FIG. 5. Energy spectra from spatiotemporal patterns. (a-d) Panels correspond to the analysis of simulations of the KSE, while (e-h) correspond to the analysis of an ABL. (a,e) Spatio-temporal patterns under study, originated in the phase field ψ of the KSE (a) and in the fluorescence profile of the AN along the inner wall in a $200\mu\text{m}$ -wide annulus with an inner radius $R_i = 150\mu\text{m}$ (e). A sample of the spatial patterns is shown in (b) and (f). L is the width of the respective kymographs. The time-averaged spatial correlation functions, C , are shown in (c) and (g), and the corresponding Fourier transforms are shown in (d) and (h). The axes are renormalized with the maximum kinetic energy and corresponding wavenumber in the spectra. The expected k^{-4} scaling is shown in panel (d), while two regimes are observed in (h) with $\alpha \sim 1.7$ and $\beta \sim 3.4$.

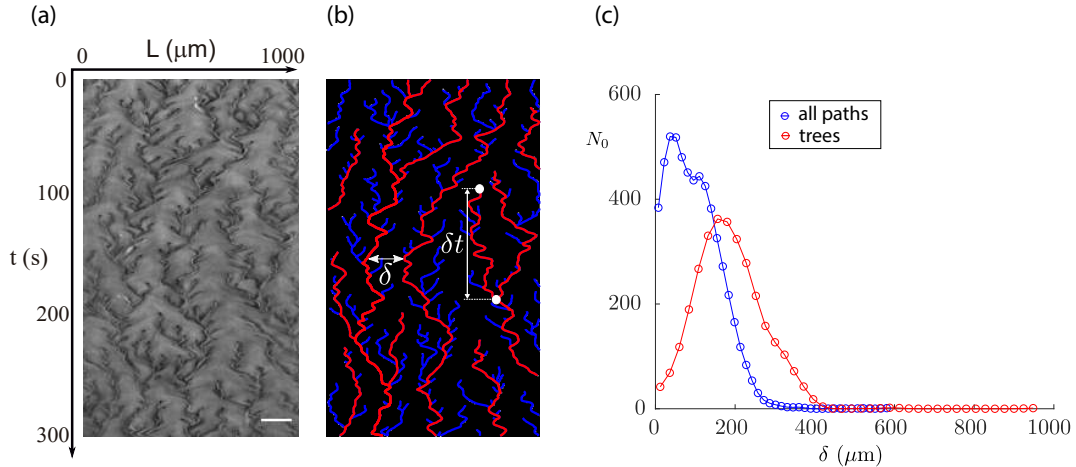


FIG. 6. Statistical description of wall defects. (a) Kymograph of the fluorescence intensity of the AN along the inner wall in a $200\mu\text{m}$ -wide annulus with an inner radius $R_i = 150\mu\text{m}$. (b) Skeletonized rendering of the kymograph where long-lived trees have red trajectories while short-lived branches have blue trajectories. (c) Distribution of distance between neighboring trees and branches combined, and between trees only.

of trees only, the distribution features a maximum at $\delta_{tt} = 192 \pm 10 \mu\text{m}$, which measures the mutual separation between long-lived trees. An interesting signature of the kymograph structure is given by the approximate relation $\delta_{tt} \approx (\delta_{bt} + 2\delta)$. To our understanding, this result clearly illustrates the particular unidimensional regulation of wall defect density that comes to play: while the distance between long-lived defects appears regulated by a well-defined wave-length, such a periodic spacing is disrupted by frequent nucleations on both sides of the trees, as described in Sec. III B. Because these nucleations occur at distances smaller than the natural tree spacing, the resulting defects are necessarily unstable and short-lived.

IV. DISCUSSION AND CONCLUDING REMARKS

Our work provides a new perspective in the study of ANs. It demonstrates a previously unrecognized role of confining walls in building up boundary layers that accumulate equal sign topological defects. Moreover it points to new experimental possibilities of controlling active flows through simple boundary interventions.

Although the spatial partition of bulk defects in active nematics induced by curvature has been recently analyzed from experiments [27] and theory [43], our results demonstrate that boundary-residing defects display profound alterations of their intrinsic symmetries and build up stresses, sensibly different from their bulk counterparts. This is a new aspect that adds to the versatility of active nematic flows. This principle has been demonstrated independently of the particular confining geometry since both curved and planar walls behave similarly in this particular respect. At the same time, we have proved a true “boundary-layer” effect, since the material residing close to the wall appears largely protected from the bulk, while the latter is profoundly affected by the boundary. Actually, the turbulent-like large-scale flows may be largely tamed by boundaries under particularly strong confinement.

Two observed features are particularly intriguing case studies in relation to well-established paradigms in ANs. In general grounds, it is surprising that equal-charge defects annihilate. Moreover, in the context of AN defects,

the apparent autonomous motion of negative wall defects, normally advected by the flow, is also remarkable. We have shown that this unusual behavior stems from the particular polar-like symmetry of wall defects that ultimately renders the boundary layer topologically polarized.

The referred dynamics of boundary defects is unpredictable, defying the common characterization in terms of the conventionally introduced active length and time scales characteristic of unconfined ANs. A promising interpretation is provided by classical ideas on spatio-temporal chaos applied to pattern forming systems, and associated descriptions in terms of dynamics with a minimum number of degrees of freedom (best exemplified by the KSE approach). Whether this resemblance is purely accidental or, rather a clue to look deeply for some universal behavior in disparate classes of non-equilibrium systems (pattern forming vs. active), is something to be elucidated. We ambition that this report could motivate further studies along this direction.

ACKNOWLEDGMENTS

The authors are indebted to the Brandeis University MRSEC Biosynthesis facility for providing the tubulin. We thank M. Pons, A. LeRoux, and G. Iruela (Universitat de Barcelona) for their assistance in the expression of motor proteins. We also thank P. Ellis and A. Fernandez-Nieves for kindly sharing all their image processing and defect detection algorithms. J.I.-M., and F.S. acknowledge funding from MINECO (project FIS2016-78507-C2-1-P, AEI/FEDER, EU). J.H. acknowledges funding from the European Union’s Horizon 2020 research and innovation program under grant agreement no. 674979-NANOTRANS. T. L.-L. acknowledges funding from the French Agence Nationale de la Recherche (Ref. ANR-13-JS08-006-01) and from the 2015 Grant SESAME MIL-AMIFAB (Ref. 15013105) for the acquisition of a Nanoscribe GT Photonic Professional device. Brandeis University MRSEC Biosynthesis facility is supported by NSF MRSEC DMR-1420382. Discussions with H. Chaté on the application of the KS equation are acknowledged. We also thank Olivier Dauchot for preliminary discussions on the KS equation.

-
- [1] H. Lamb, *Hydrodynamics* (Cambridge University Press, 1993).
 - [2] R. Hunter, *Foundations of Colloid Science* (Oxford University Press, 2000).
 - [3] A. Doostmohammadi, J. Ignés-Mullol, J. M. Yeomans, and F. Sagués, Active nematics, *Nature Communications* **9**, 3246 (2018).
 - [4] T. Sanchez, D. T. Chen, S. J. DeCamp, M. Heymann,

- and Z. Dogic, Spontaneous motion in hierarchically assembled active matter, *Nature* **491**, 431 (2012).
- [5] G. Henkin, S. J. DeCamp, D. T. Chen, T. Sanchez, and Z. Dogic, Tunable dynamics of microtubule-based active isotropic gels, *Philos. Trans. A: Math. Phys. Eng. Sci.* **372**, 0142 (2014).
- [6] P. Guillamat, J. Ignés-Mullol, S. Shankar, M. C. Marchetti, and F. Sagués, Probing the shear viscosity of

- an active nematic film, *Phys. Rev. E* **94**, 060602 (2016).
- [7] J. Hardoüin, R. Hughes, A. Doostmohammadi, J. Laurent, T. Lopez-Leon, J. M. Yeomans, J. Ignés-Mullol, and F. Sagués, Reconfigurable Flows and Defect Landscape of Confined Active Nematics, *Commun. Phys.* **2**, 121 (2019).
- [8] J. Prost, F. Jülicher, and J. F. Joanny, Active gel physics, *Nature Physics* **11**, 111 (2015).
- [9] D. Needleman and Z. Dogic, Active matter at the interface between materials science and cell biology, *Nature Reviews Materials* **2**, 10.1038/natrevmats.2017.48 (2017).
- [10] S. J. DeCamp, G. S. Redner, A. Baskaran, M. F. Hagan, and Z. Dogic, Orientational order of motile defects in active nematics, *Nat. Matter.* **14**, 1110 (2015).
- [11] P. Guillamat, J. Ignés-Mullol, and F. Sagués, Control of active liquid crystals with a magnetic field, *Proc. Natl. Acad. Sci.* **113**, 5498 (2016).
- [12] P. Guillamat, J. Ignés-Mullol, and F. Sagués, Taming active turbulence with patterned soft interfaces, *Nat. Commun.* **8** (2017).
- [13] L. M. Lemma, S. J. Decamp, Z. You, G. L., and Z. Dogic, Soft Matter 2D active nematics †, *Soft Matter* **15**, 3264 (2019).
- [14] L. M. Pismen, Dynamics of defects in an active nematic layer, *Phys. Rev. E* **88**, 050502 (2013).
- [15] L. Giomi, M. J. Bowick, X. Ma, and M. C. Marchetti, Defect annihilation and proliferation in active nematics, *Phys. Rev. Lett.* **110**, 228101 (2013).
- [16] X. Q. Shi and Y. Q. Ma, Topological structure dynamics revealing collective evolution in active nematics, *Nature Communications* **4**, 3013 (2013).
- [17] S. P. Thampi, R. Golestanian, and J. M. Yeomans, Instabilities and topological defects in active nematics, *Europhys. Lett.* **105**, 18001 (2014).
- [18] E. J. Hemingway, P. Mishra, M. C. Marchetti, and S. M. Fielding, Correlation lengths in hydrodynamic models of active nematics, *Soft Matter* **12**, 7943 (2016), [arXiv:1604.01203](https://arxiv.org/abs/1604.01203).
- [19] L. M. Pismen and F. Sagués, Viscous dissipation and dynamics of defects in an active nematic interface, *Euro. Phys. J. E* **40**, 92 (2017).
- [20] S. Shankar, S. Ramaswamy, M. C. Marchetti, and M. J. Bowick, Defect Unbinding in Active Nematics, *Physical Review Letters* **121**, 108002 (2018).
- [21] L. Giomi, Geometry and topology of turbulence in active nematics, *Phys. Rev. X* **5**, 031003 (2015).
- [22] J. Urzay, A. Doostmohammadi, and J. M. Yeomans, Multi-scale statistics of turbulence motorized by active matter, *Journal of Fluid Mechanics* **822**, 762 (2017), [arXiv:1705.03703](https://arxiv.org/abs/1705.03703).
- [23] R. Alert, J.-F. Joanny, and J. Casademunt, Universal scaling of active nematic turbulence, *Nature Physics* 10.1038/s41567-020-0854-4 (2019), [arXiv:1906.04757](https://arxiv.org/abs/1906.04757).
- [24] B. Martínez-Prat, J. Ignés-Mullol, J. Casademunt, and F. Sagués, Selection mechanism at the onset of active turbulence, *Nature Physics* **15**, 362 (2019).
- [25] M. C. Cross and P. C. Hohenberg, Pattern formation outside of equilibrium, *Rev. Mod. Phys.* **65**, 851 (1993).
- [26] C. A. Schneider, W. S. Rasband, and K. W. Eliceiri, Nih image to imagej: 25 years of image analysis, *Nature Methods* **9**, 671 (2012).
- [27] P. W. Ellis, D. J. G. Pearce, Y.-W. Chang, G. Goldsztein, L. Giomi, and A. Fernández-Nieves, Curvature-induced defect unbinding and dynamics in active nematic toroids, *Nat. Phys.* **14**, 85 (2018).
- [28] Edward Renshaw a solution to the kuramoto-sivashinski equation, <https://github.com/E-Renshaw/kuramoto-sivashinsky.com>.
- [29] R. Voituriez, J. F. Joanny, and J. Prost, Spontaneous flow transition in active polar gels, *Europhysics Letters (EPL)* **70**, 404 (2005).
- [30] S. Ramaswamy, The Mechanics and Statistics of Active Matter, *Annu. Rev. Condens. Matter Phys.* **1**, 323 (2010).
- [31] S. Chen, P. Gao, and T. Gao, Dynamics and structure of an apolar active suspension in an annulus, *Journal of Fluid Mechanics* **835**, 393 (2018).
- [32] A. Opathalage, M. M. Norton, M. P. N. Juniper, B. Langeslay, S. A. Aghvami, S. Fraden, and Z. Dogic, Self-organized dynamics and the transition to turbulence of confined active nematics, *Proceedings of the National Academy of Sciences* **116**, 4788 (2019).
- [33] T. Sanchez, D. Welch, D. Nicastro, and Z. Dogic, Cilia-like beating of active microtubule bundles, *Science* **333**, 456 (2011).
- [34] I. S. Aranson and L. Kramer, The world of the complex ginzburg-landau equation, *Reviews of Modern Physics* **74**, 99 (2002).
- [35] W. Wittenberg, R and P. Holmes, Scale and space localization in the Kuramoto-Sivashinsky equation, *Chaos* **9**, 452 (1999).
- [36] Y. Kuramoto, Diffusion-induced chaos in reaction systems, *Progress of Theoretical Physics Supplement* **64**, 346 (1978).
- [37] Y. Kuramoto and T. Tsuzuki, Persistent propagation of concentration waves in dissipative media far from thermal equilibrium, *Progress of theoretical physics* **55**, 356 (1976).
- [38] P. Manneville, The kuramoto-sivashinsky equation: a progress report, in *Propagation in systems far from equilibrium* (Springer, 1988) pp. 265–280.
- [39] G. Sivashinsky, Nonlinear analysis of hydrodynamic instability in laminar flames—i. derivation of basic equations, *Acta astronautica* **4**, 1177 (1977).
- [40] G. Sivashinsky, Diffusional-thermal theory of cellular flames, *Combustion Science and Technology* **15**, 137 (1977).
- [41] S. Toh, Statistical model with localized structures describing the spatio-temporal chaos of kuramoto-sivashinsky equation, *Journal of the Physical Society of Japan* **56**, 949 (1987), <https://doi.org/10.1143/JPSJ.56.949>.
- [42] Y. Pomeau, A. Pumir, and P. Pelce, Intrinsic stochasticity with many degrees of freedom, *Journal of Statistical Physics* **37**, 39 (1984).
- [43] D. J. Pearce, P. W. Ellis, A. Fernández-Nieves, and L. Giomi, Geometrical Control of Active Turbulence in Curved Topographies, *Physical Review Letters* **122**, 168002 (2019), [arXiv:1909.01115](https://arxiv.org/abs/1909.01115).

SUPPLEMENTARY MATERIAL**Active Boundary Layers**

Jérôme Hardoüin *et al.*

Supplementary Figures

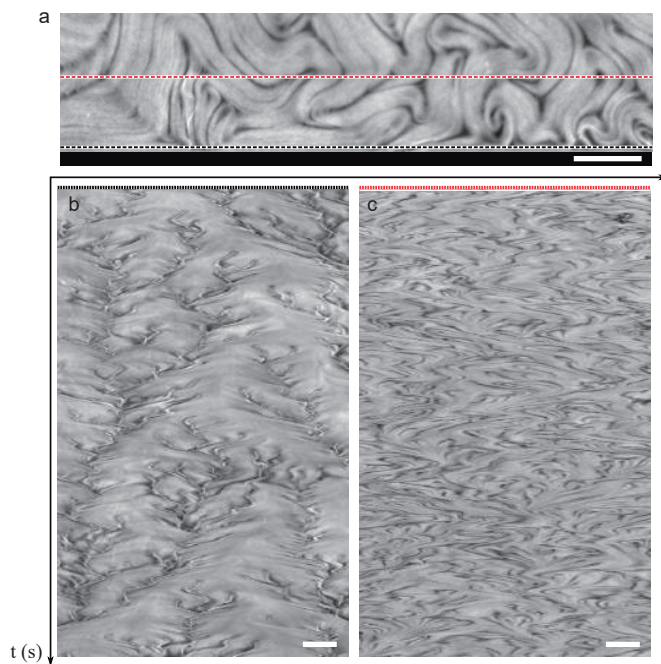


FIG. S1. Penetration depth of wall defects in an active nematic near a flat wall. Scale bars, $100 \mu\text{m}$. (a) Fluorescence micrograph. The wall is marked by the black rectangle. The black and red dotted lines correspond to the pixel arrays used to compute the space-time plots of the dynamics close (b) and far (c) from the wall, respectively.

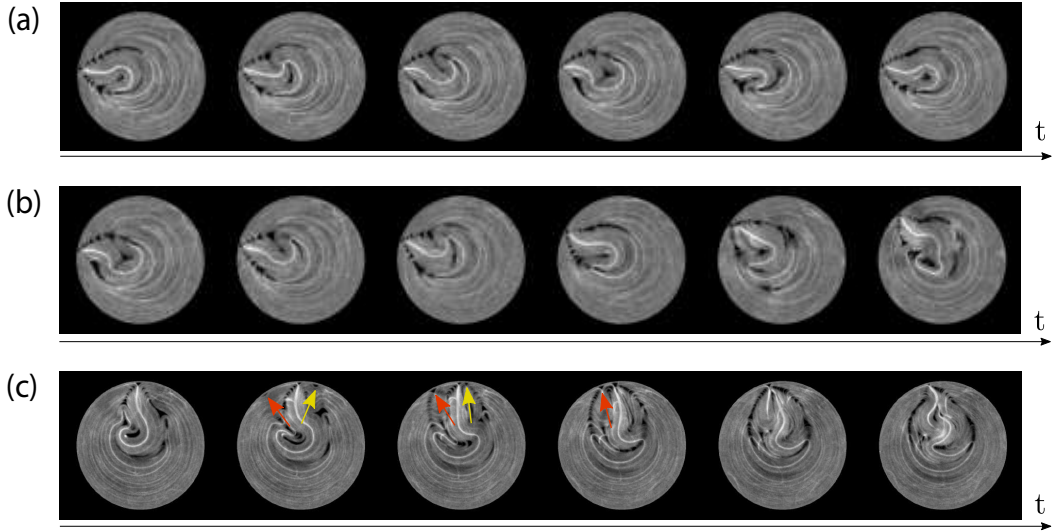


FIG. S2. Dynamics of isolated wall-defects in a disk. Fluorescence micrograph of active nematics confined inside a disk of $170 \mu\text{m}$ radius. (a) Time lapse showing transversal fluctuations of a wall-defect with a plume emerging from it. The interval between two frames is 2 s. (c) Time lapse showing the slow drift of the defect along the wall. The interval between two frames is 25 s. (b) Time lapse showing two wall defect nucleation event followed by their merging into a single one. The newborn defects are pointed by coloured arrows. The interval between two frames is 2 s.

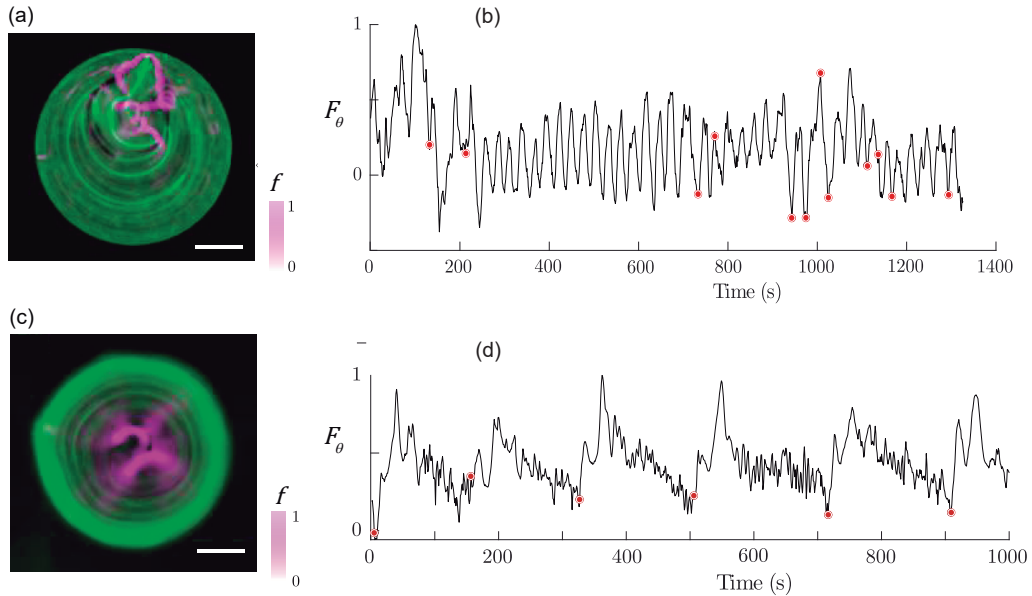


FIG. S3. Tangential forces and defect nucleation in active nematics confined in a disk using two different protocols: (a,b) correspond to data in this work, and (c,d) correspond to a video from Opathalage et al. [32] (a, c) Fluorescence micrographs of active nematics (green pseudo-color) with the corresponding map of $f = |\nabla \cdot Q|$ (pink color map). (b, d) Spatially-integrated active force, $F_\theta = \int(\mathbf{e}_\theta \cdot \nabla \cdot \mathbf{Q})d\mathbf{r}$ as a function of time. Nucleation events are marked with orange disks. Scale bars are $100 \mu\text{m}$ (a) and $20 \mu\text{m}$ (c).

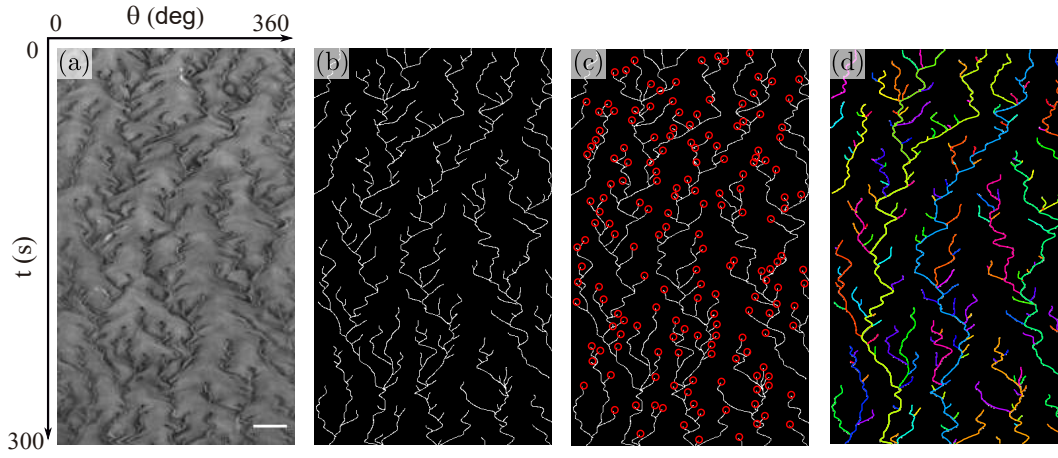


FIG. S4. Branches and trees in active nematics. (a) Space-time plot of the fluorescence intensity at the inner wall of a $200\ \mu\text{m}$ wide active nematic annulus with inner radius $150\ \mu\text{m}$. Time goes downwards. Scale bar: $200\ \mu\text{m}$. (b) Binary skeletonisation of the localized structures in (a). (c) Defect nucleation events, defined as the beginning of a white line in (b). (d) Tracking of defect paths.

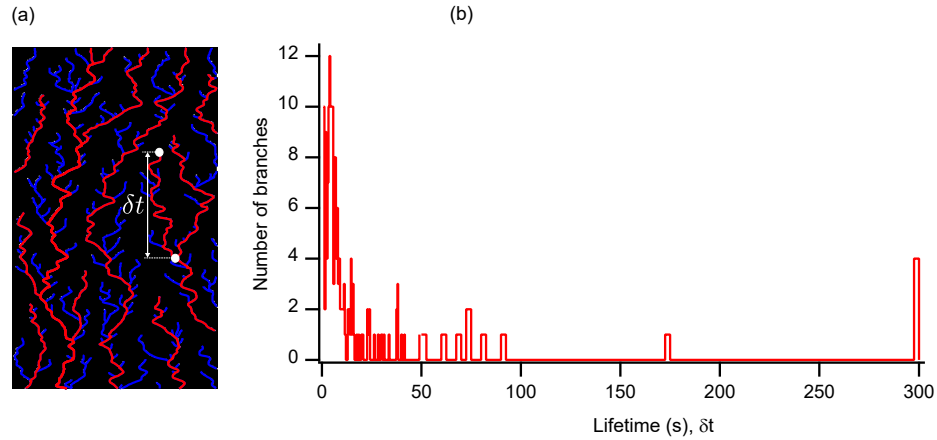
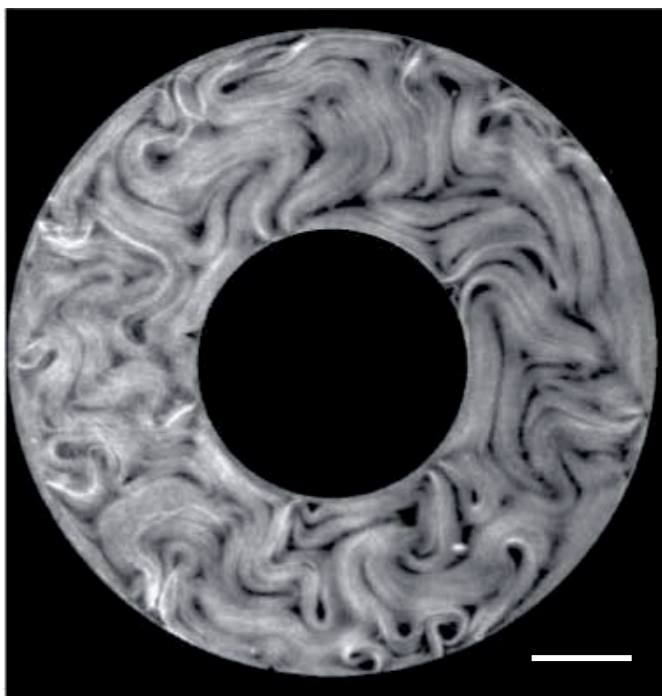
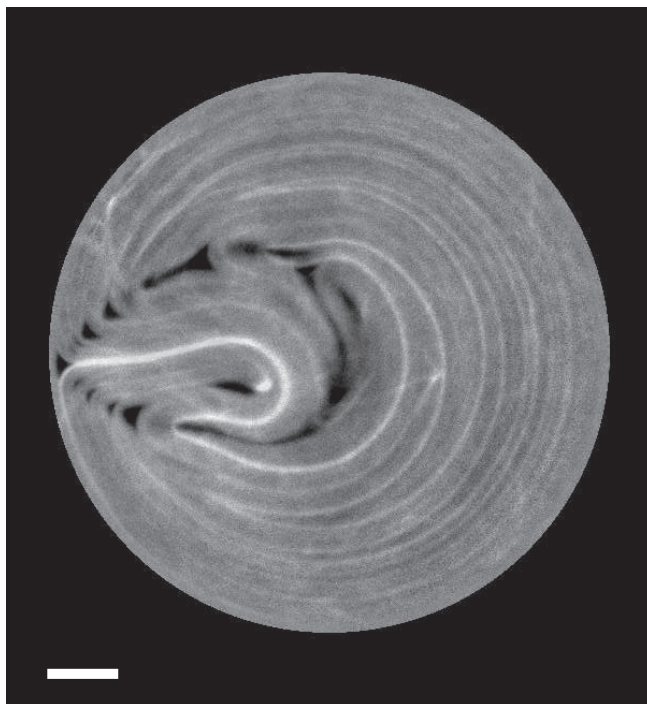


FIG. S5. Lifetime distribution of trees and branches. (a) Skeletonized and color-coded wall-defect trajectories in a kymograph showing long trees in red and short branches in blue. This classification has been made by selecting a threshold lifetime of 50s above which branches become trees, as suggested by the statistical analysis in (b). The lifetime δt is defined as the time between the nucleation and the merging of a given structure. Statistics in this experiment are obtained over 169 branches and 12 trees.

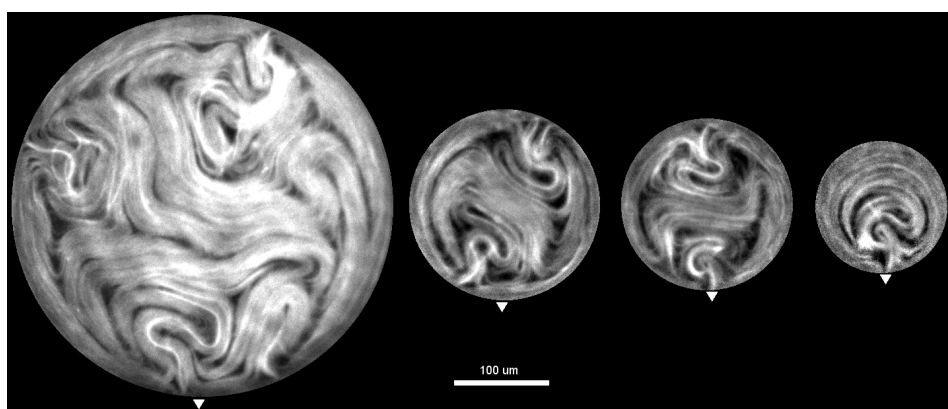
Supplementary Movie Captions



Movie S1. Active nematic confined to a ring-shaped channel. Scale bar: $100\mu\text{m}$. Active boundary layers are observed on the inner and on the outer ring walls.



Movie S2. Active nematic confined to a circular pool. Scale bar: $100\mu\text{m}$. A single boundary defect is observed most of the time, determining the flow inside the pool.



Movie S3. Active nematic confined to circular pools of different sizes with an etched indentation (white triangle).